Internal structure of sponge glass fiber revealed by ptychographic nanotomography

CrossMark

Mie E. Birkbak [a], Manuel Guizar-Sicairos [b], Mirko Holler [b], Henrik Birkedal [a,*]

[a] iNANO and Department of Chemistry, Aarhus University, 14 Gustav Wieds Vej, 8000 Aarhus, Denmark
[b] Paul Scherrer Institut, 5332 Villigen PSI, Switzerland

A B S T R A C T

Sponge glass spicules have solicited great interest due to their mechanical and optical properties. Herein we use ptychographic nanotomography to obtain detailed insights into the internal structure of an anchor spicule from the Venus flower basket. The obtained dataset has 90 nm resolution in 3D and provides quantitative determination of the electron density. The data reveal significant variations in electron density across the spicule. The central organic filament is found to be slightly but significantly displaced from the spicule central axis. Analysis of the electron density affords an estimate of a protein volume fraction in the organic filament of about 70%. In the highly mineralized part of the spicule, the electron density is seen to display circular symmetry and be neigh independent of position along the spicule long axis. Variations in the electron density beyond those included in current models of spicule mechanics are observed.

© 2016 Elsevier Inc. All rights reserved.

1. Introduction

Biology makes many advanced materials (Meyers et al., 2013). The deep sea hexactinellid glass sponge *Euplectella aspergillum*, also known as the Venus flower, has an intricate glass fiber based skeleton shown in Fig. 1A. The skeleton features a complex architecture of interwoven fibers (Aizenberg et al., 2005; Weaver et al., 2007, 2010; Woesz et al., 2006). The organism is anchored in the sea bottom with anchor spicules, Fig. 1B, that are the focus of the present work. The spicules have a laminated architecture that leads to excellent fiber-optical properties (Aizenberg et al., 2004; Sundar et al., 2003). It contains a ∼0.5 µm organic axial filament (OF), a smooth central region (CC) 15–25 µm in diameter, embedded in the laminated striated shell (SS) composed of 0.8–1 µm width sheets (Aizenberg et al., 2004; Weaver et al., 2007). The silica framework consists of consolidated silica nanoparticles (Weaver et al., 2007), possibly consisting of even smaller primary particles (Woesz et al., 2006). This laminated structure results in spatially modulated mechanical properties and affords increased fracture resistance (Kolednik et al., 2011; Miserez et al., 2008; Monn et al., 2015; Weaver et al., 2007). The organic filament serves as template to the silica structure and has been reported to be square in *E. aspergillum* (Weaver et al., 2007). Understanding the structure of these complex structures is highly challenging and has rendered etching or other destructive techniques necessary. These methods have not allowed quantitative assessment of the variations in matter density within the spicule, which in turn is essential for understanding spicule properties. Herein, we instead employ ptychography to shed light on the internal structure of a *E. aspergillum* anchor spicule.

Ptychography is a coherent diffractive imaging technique where an image is constructed from coherent diffraction patterns taken from positions of overlapping illumination (Rodenburg and Faulkner, 2004). By combining several such images collected at different view angles of the specimen, a 3D view of the internal structure can be obtained by tomographic reconstruction (Dierolf et al., 2010). The resolution is ultimately limited by the scattering power of the specimen and the images provide quantitative information on the electron density within the specimen (Diaz et al., 2012). 3D resolution down to 16 nm has been reported (Holler et al., 2014). The technique is thus ideally suited to study complex nanostructured biological materials such as bone (Dierolf et al., 2010) or silk fibers (Esmaeili et al., 2013).

2. Materials and methods

E. aspergillum material was obtained from a shell vendor and an anchor spicule was extracted, cut by a blade and mounted by a micromanipulator using UV-curing glue (APM UV cure handheld

---

* Corresponding author.
   E-mail address: hbirkedal@chem.au.dk (H. Birkedal).
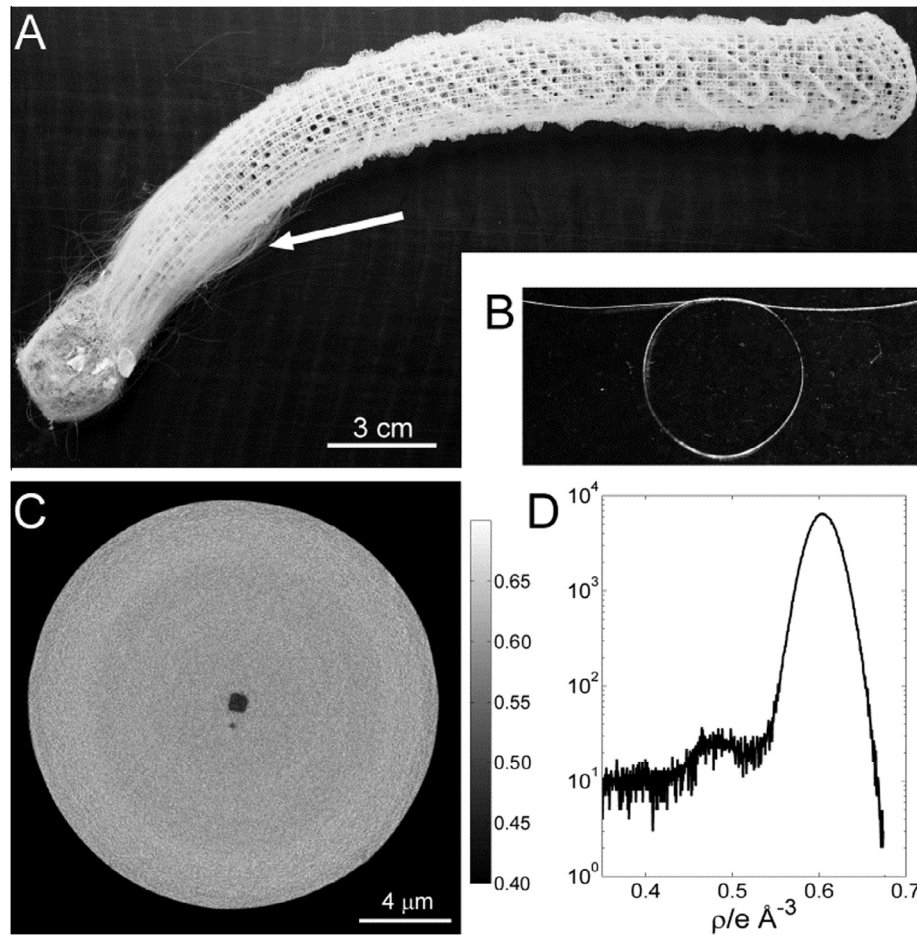
Fig. 1. The Venus flower basket, *Euplectella aspergillum* (A), has anchor spicules one of which is shown with a knot tied onto it in panel (B). A fragment of such a spicule was studied using ptychography. (C) Shows a reconstructed tomographic slice of electron density while panel (D) shows a histogram of the electron density in the slice shown in (C).

curing system, APM Technica, Heerbrugg, Switzerland; UV Glue Norland Optical Adhesive 61, Cranbury, NJ, USA) onto a sample mount for ptychography.

The ptychographic nanotomography measurements were carried out at the cSAXS beamline, Swiss Light Source, Paul Scherrer Institut, Switzerland using 6.2 keV photon energy with an interferometrically controlled 3D scanning stage (Holler et al., 2012, 2014). The sample was scanned across a coherent X-ray beam approximately 4 µm in diameter. The measurement was carried out as described by Holler et al. (2014) and the 2D projection images were aligned using methods based on 3D consistency (Guizar-Sicairos et al., 2015, 2011) and used to obtain a high-resolution 3D electron density map of the sample. The field of view was of 30 µm × 20 µm with a scan following a Fermat spiral pattern (Huang et al., 2014) with an average step size of 1.2 µm. This scan was repeated at 500 equally spaced angular orientations that spanned a range from 0° to 180°. At each scanning point, diffraction patterns were measured with a Pilatus photon-counting detector (Henrich et al., 2009) with a 0.1 s exposure time. Ptychographic reconstructions were carried out using the difference map algorithm with a maximum likelihood refinement (Guizar-Sicairos and Fienup, 2008; Thibault and Guizar-Sicairos, 2012) resulting in 2D reconstructions with a pixel size of 21.4 nm. Tomographic synthesis was carried out with projection alignment and postprocessing as described in (Guizar-Sicairos et al., 2011) including a refinement of projection alignment using tomographic consistency (Guizar-Sicairos et al., 2015).

The ptychographic nanotomography data set contained 650 slices with a voxel size of 21.4 nm, with the slices being perpendicular to the rotation axis which was approximately aligned with the filament axis. The resolution was determined by Fourier shell correlation (Holler et al., 2014; van Heel and Schatz, 2005) and edge detection analysis to be ~90 nm.

The reconstructed electron density stack was tilted numerically based on the position of the spicule centroid that was determined in each image using custom software. Thereafter, the image stack axis was parallel to the spicule long axis. This image stack was used for all further analysis.

The reconstructed electron density was recast into azimuthally and radially integrated datasets. This was done by transforming the reconstructed slice from cartesian to polar coordinates (Almer and Stock, 2005).

To analyze the shape of the central filament, we use a measure of squareness: for a rectangle with sidelengths $\alpha - \delta$ and $\alpha + \delta$, the perimeter is $P = 4\ \alpha$ while the area is $A = \alpha^2 - \delta^2$ so that $S = \sqrt{A}/(P/4)$ becomes $S = \sqrt{1 - (\delta/\alpha)^2}$. Thus for a rectangle, S is always smaller than 1 reaching 1 for square.

3. Results and discussion

The ptychographic data allow for the first time to provide high resolution, 3D structural data on sponge spicule internal structure. Fig. 1C shows a single slice through the spicule. The electron den-
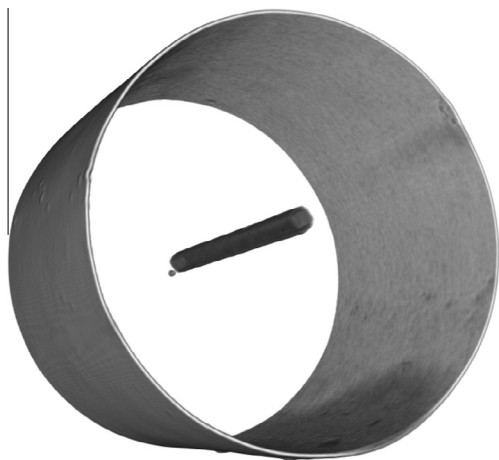
Fig. 2. Surface rendering of spicule surface featuring exterior and interior surfaces. The latter is defined as the surface between the highly mineralized regions and regions with electron densities similar to the OF; note the small defect to the left of the OF.

sity is determined on an absolute scale by ptychographic nanotomography (Diaz et al., 2012), which is a distinct advantage of this imaging technique. The reconstructed electron density clearly features the central OF as an area of lower electron density that is also visible as a small secondary maximum around 0.48 e/Å^3 in the electron density histogram displayed in Fig. 1D.

There is a small secondary region of low electron density present in this image. It forms a small isolated low density cluster as shown in the surface renderings in Fig. 2, reflecting the fact that biological materials typically are not perfect. Such features are unlikely to be discovered by other imaging techniques such as electron microscopy that in practice often are restricted to a limited number of slices. The reconstructed surfaces show that there

is a relatively high degree of overall uniformity with minor variations of the surface.

Surprisingly, the center of the filament and the spicule did not coincide in position but were 0.28(2) μm apart on average, with the number in parenthesis representing the standard uncertainty on the last digit. This was much larger than the RMS deviation of the filament and spicule around their respective medians (0.008 and 0.025 μm, respectively). This suggests that while the central filament structure is essential as an initial template for spicule development, it does not fully determine the growth process. Offset in filament and OF center has previously been observed in the giant anchor spicule of *Monorhaphis chuni.* This animal uses a single giant spicule to anchor to the sea floor. In that case, the offset was assigned to an adaption to bending stress from prevailing sea currents (Miserez et al., 2008). We suggest that similar effects may be at play for *E. aspergillum* though to a smaller degree that could only be revealed by the present very high resolution imaging approach.

The average filament cross-sectional area was 0.580(15) μm^2 while the corresponding average spicule cross-sectional area was 251.4(5) μm^2 so that the central filament only makes up 0.23% of the total spicule volume. The shape of the filament cross sections was found not to be perfectly rectangular. Indeed perusal of the images showed that the OF sides had a tendency to be convex. A measure of the deviation from a square shape can be obtained from the ratio of square root of the area, A, and the average side length obtained from the perimeter, P: $S = A^{1/2}/(P/4)$. This measure is 1 for a perfect square while it is smaller than 1 for a rectangle. For the OF we found an average value of 0.94 ± 0.04.

The average electron density in the OF was 0.4813 e/Å^3, while that of the surrounding more highly mineralized material was 0.6039 e/Å^3. The average electron density over the whole volume of the spicule was 0.6008 e/Å^3 because there were additional low-electron density regions on the very surface of the spicule. The electron density of the highly mineralized part can be compared *e.g.* to the electron density of geological silica, which is
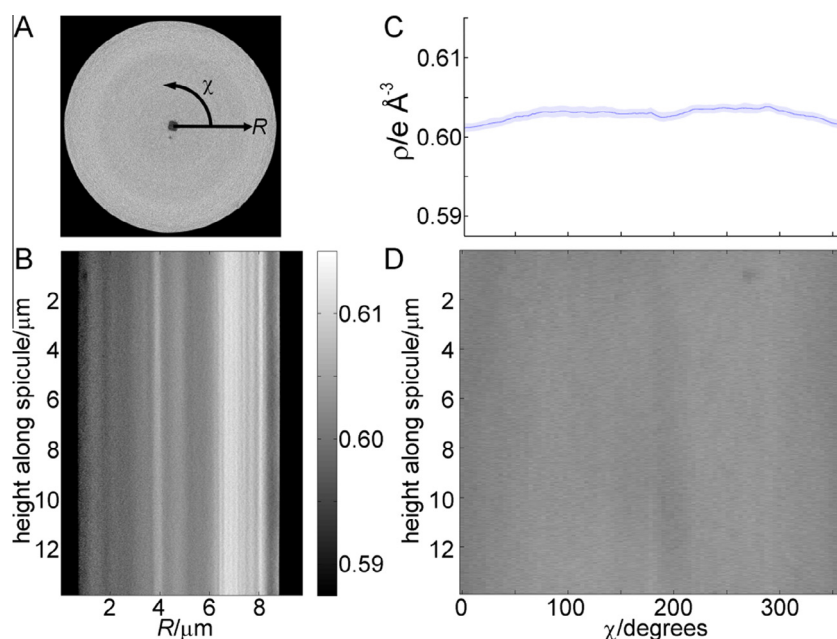
Fig. 3. The electron density in the anchor spicule varies only little along spicule long axis and azimuthal angle. (A) Definition of χ and R, the azimuthal angle and radial distance, respectively shown on the slice from Fig. 1C. (B) Gray scale image showing the electron density integrated over the azimuthal angle as a function distance from spicule centroid, R, and height along spicule axis (corresponding to slice number). (C and D) The electron density is almost independent of azimuthal angle (χ). (D) Shows a gray scale image of the intensity averaged over distance from the centroid excluding the OF while (C) shows the mean over the spicule height with the light blue bar representing the standard devation.
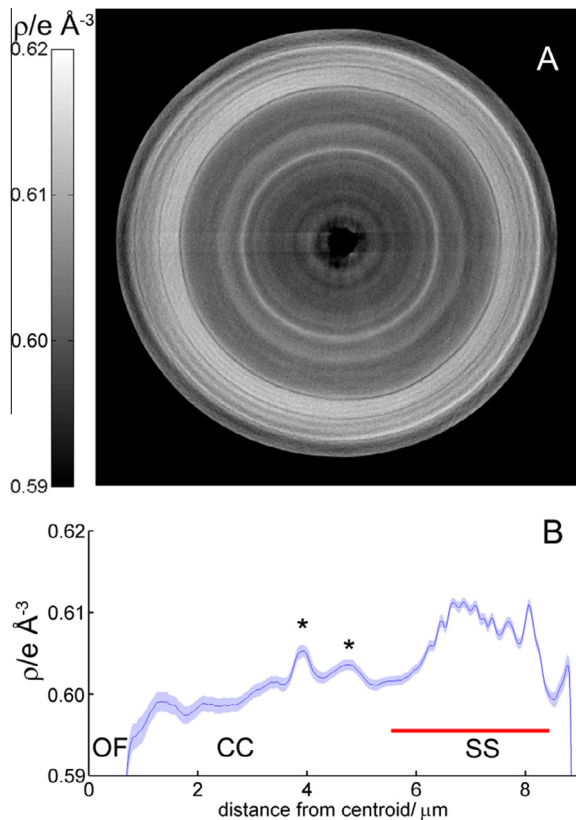
Fig. 4. Electron density averaged over the spicule axial length. (A) Shows the 2D electron density distribution while (B) shows the electron density as a function of radial distance from the spicule centroid obtained by azimuthally averaging over the electron density shown in (A). The thin dark line is the average, while the light band displays the associated standard uncertainty. The * indicate two maxima in the central region (CC) while the red line indicates the striated shell (SS) region. Note that the electron density has been displayed as to highlight variations in the high density part of the spicule and thus does not feature the OF.

0.66 e/Å^3 based on a density of 2.19 g/cm^3. This difference must originate from the presence of water, biomolecules and possibly nanoscale porosities occurring at a length scale smaller than the resolution. Assuming that the density difference in the OF compared to the bulk is due to the OF being a high-protein-content composite and using 0.43 e/Å^3 as an estimate of a protein electron density (Yang et al., 2009), allows us to grossly estimate the protein volume fraction to be ~77% in the OF. This is an overestimate due to the fact that the OF region also contains higher amounts of sodium than the surroundings (Aizenberg et al., 2004), but the value does show that the OF indeed contains a large volume fraction of protein matter.

The geometric features of the spicule determined by the 3D ptychographic nanotomography were fully consistent with observations on polished sections and fracture surfaces made with SEM (Figs. S1 and S2).

The individual slices clearly display variations in electron density in the striated shell region, Fig. 1C. However, the electron density is almost constant the spicule length as shown in Fig. 3. The electron density around the disk can be obtained by integrating over the azimuthal angle, Fig. 3A, and the resulting electron density map as a function of radial distance from the centroid and height along the spicule is remarkably independent of height, Fig. 3B. By averaging over the radial coordinate, we further found that only very minor azimuthal dependencies. This is shown in Fig. 3C and D.

The negligible variation in electron density along the spicule length allowed calculating an average image by averaging along the filament axial length, which is shown in Fig. 4A. The electron density is clearly varying significantly with radial distance from the organic filament. To quantify this, the radial dependence of the electron density was calculated by averaging over the azimuthal angle. The average electron density is shown in Fig. 4B.

The striated region (SS in Fig. 4B) is seen 6–8 μm from the disk centroid. The electron density is higher in the SS than in the CC, 0.6065 vs. 0.6006 e/Å^3 on average, even though the former contains thin sheets of organic material. This may originate from changes in water content and/or degree of sodium substitution, which is known also to be present in the spicules (Aizenberg et al., 2004). We observe several additional maxima in the electron density closer to the OF indicated by stars in Fig. 4B. This is in apparent contrast to the identification of a single striated region based on SEM fracture images (Monn et al., 2015) suggesting that these variations in electron density are rather due to changes in glass matrix composition than the presence of additional organic matrix variations. In the SS we identified 10 peaks in the electron density corresponding to ~9 interspersing organic layers. The thickness of the highly mineralized layers was obtained by fitting Gaussian peaks to the SS region of the electron density. Average FWHM of 0.22 μm ranging from 0.11 to 0.45 μm was obtained. These values are in good agreement with those determined on fractured spicules (Aizenberg et al., 2004).

The current determination of variations in the electron density has important ramifications for our understanding of spicule properties. The visible light refractive index is highest in the OF followed by the SS with the CC having the lowest value (Aizenberg et al., 2004). The difference between SS and CC has been suggested to be due to differences in silica density (Aizenberg et al., 2004). This is confirmed by the present quantitative measurements of electron density. Current models of how the laminated structure increase fracture toughness (Kolednik et al., 2011; Miserez et al., 2008; Woesz et al., 2006) and how it is related to load transfer between skeleton and sediment (Monn et al., 2015) all base themselves on the assumption that the silica matrix is homogeneous. This has led to models that capture many features of the macro- and micro-mechanical properties of the spicules. The present work shows significant variations in matrix composition across the spicule cross-section also in the CC. Whether this observation in turn demands refinements of such mechanical models requires further mechanical investigations with sub-micrometer resolution. Methods for such investigations are emerging (Zhang et al., 2015).

4. Conclusion

In conclusion, we illustrated how novel quantitative X-ray imaging tools such as ptychography provide detailed insights into complex biological materials especially due to their ability to quantitatively determine the electron density inside materials. This allowed establishing that the OF is not centered in the spicule and that there are variations in the electron density beyond those included in the current models of spicule mechanics (Monn et al., 2015). Our results clearly highlight the need for high-resolution 3D imaging techniques when studying complex hierarchical composite materials.

Acknowledgments

Appendix A. Supplementary data

Supplementary data associated with this article can be found, in the online version, at http://dx.doi.org/10.1016/j.jsb.2016.02.006.

References

Aizenberg, J., Sundar, V.C., Yablon, A.D., Weaver, J.C., Chen, G., 2004. Biological glass fibers: Correlation between optical and structural properties. Proc. Natl. Acad. Sci. U.S.A. 101, 3358–3363.

Aizenberg, J., Weaver, J.C., Thanawala, M.S., Sundar, V.C., Morse, D.E., Fratzl, P., 2005. Skeleton of *Euplectella* sp.: Structural hierarchy from the nanoscale to the macroscale. Science 309, 275–278.

Almer, J.D., Stock, S.R., 2005. Internal strains and stresses measured in cortical bone via high-energy X-ray diffraction. J. Struct. Biol. 152, 14–27.

Diaz, A., Trtik, P., Guizar-Sicairos, M., Menzel, A., Thibault, P., Bunk, O., 2012. Quantitative X-ray phase nanotomography. Phys. Rev. B 85, 020104(R).

Dierolf, M., Menzel, A., Thibault, P., Schneider, P., Kewish, C.M., Wepf, R., Bunk, O., Pfeiffer, F., 2010. Ptychographic X-ray computed tomography at the nanoscale. Nature 467, 436–439.

Esmaeili, M., Fløystad, J.B., Diaz, A., Høydalsvik, K., Guizar-Sicairos, M., Andreasen, J. W., Breiby, D.W., 2013. Ptychographic X-ray tomography of silk fiber hydration. Macromolecules 46, 434–439.

Guizar-Sicairos, M., Fienup, J.R., 2008. Phase retrieval with transverse translation diversity: a nonlinear optimization approach. Opt. Express 16, 7264–7278.

Guizar-Sicairos, M., Boon, J.J., Mader, K., Diaz, A., Menzel, A., Bunk, O., 2015. Quantitative interior X-ray nanotomography by a hybrid imaging technique. Optica 2, 259–266.

Guizar-Sicairos, M., Diaz, A., Holler, M., Lucas, M.S., Menzel, A., Wepf, R.A., Bunk, O., 2011. Phase tomography from X-ray coherent diffractive imaging projections. Opt. Express 19, 21345–21357.

Henrich, B., Bergamaschi, A., Broennimann, C., Dinapoli, R., Eikenberry, E.F., Johnson, I., Kobas, M., Kraft, P., Mozzanica, A., Schmitt, B., 2009. PILATUS: a single photon counting pixel detector for X-ray applications. Nucl. Instrum. Methods Phys. Res. A 607, 247–249.

Holler, M., Raabe, J., Diaz, A., Guizar-Sicairos, M., Quitmann, C., Menzel, A., Bunk, O., 2012. An instrument for 3D X-ray nano-imaging. Rev. Sci. Instrum. 83, 073703.

Holler, M., Diaz, A., Guizar-Sicairos, M., Karvinen, P., Färm, E., Härkönen, E., Ritala, M., Menzel, A., Raabe, J., Bunk, O., 2014. X-ray ptychographic computed tomography at 16 nm isotropic 3D resolution. Sci. Rep. 4, 3857.

Huang, X., Yan, H., Harder, R., Hwu, Y., Robinson, I.K., Chu, Y.S., 2014. Optimization of overlap uniformness for ptychography. Opt. Express 22, 12634–12644.

Kolednik, O., Predan, J., Fischer, F.D., Fratzl, P., 2011. Bioinspired design criteria for damage-resistant materials with periodically varying microstructure. Adv. Funct. Mater. 21, 3634–3641.

Meyers, M.A., McKittrick, J., Chen, P.-Y., 2013. Structural biological materials: critical mechanics-materials connections. Science 339, 773–779.

Miserez, A., Weaver, J.C., Thurner, P.J., Aizenberg, J., Dauphin, Y., Fratzl, P., Morse, D. E., Zok, F.W., 2008. Effects of laminate architecture on fracture resistance of sponge biosilica: lessons from nature. Adv. Mater. 18, 1–8.

Monn, M.A., Weaver, J.C., Zhang, T., Aizenberg, J., Kesari, H., 2015. New functional insights into the internal architecture of the laminated anchor spicules of *Euplectella aspergillum*. PNAS 112, 4976–4981.

Rodenburg, J.M., Faulkner, H.M.L., 2004. A phase retrieval algorithm for shifting illumination. Appl. Phys. Lett. 85, 4795–4797.

Sundar, V.C., Yablon, A.D., Grazul, J.L., Ilan, M., Aizenberg, J., 2003. Fibre-optical features of a glass sponge. Nature 424, 899–900.

Thibault, P., Guizar-Sicairos, M., 2012. Maximum-likelihood refinement for coherent diffractive imaging. New J. Phys. 14, 063004.

van Heel, M., Schatz, M., 2005. Fourier shell correlation threshold criteria. J. Struct. Biol. 151, 250–262.

Weaver, J.C., Aizenberg, J., Fantner, G.E., Kisailus, D., Woesz, A., Allen, P., Fields, K., Porter, M.J., Zok, F.W., Hansma, P.K., Fratzl, P., Morse, D.E., 2007. Hierarchical assembly of the siliceous skeletal lattice of the hexactinellid sponge *Euplectella aspergillum*. J. Struct. Biol. 158, 93–106.

Weaver, J.C., Milliron, G.W., Allen, P., Miserez, A., Rawal, A., Garay, J., Thurner, P.J., Seto, J., Mayzel, B., Friesen, L.J., Chmelka, B.F., Fratzl, P., Aizenberg, J., Dauphin, Y., Kisailus, D., Morse, D.E., 2010. Unifying design strategies in demosponge and hexactinellid skeletal systems. J. Adhes. 86, 72–95.

Woesz, A., Weaver, J.C., Kazanci, M., Dauphin, Y., Aizenberg, J., Morse, D.E., Fratzl, P., 2006. Micromechanical properties of biological silica in skeletons of deep-sea sponges. J. Mater. Res. 21, 2068–2078.

Yang, S., Park, S., Makowski, L., Roux, B., 2009. A rapid coarse residue-based computational method for X-ray solution scattering characterization of protein folds and multiple conformational states of large protein complexes. Biophys. J. 96, 4449–4463.

Zhang, S., Bach-Gansmo, F.L., Xia, D., Besenbacher, F., Birkedal, H., Dong, M., 2015. Nanostructure and mechanical property of the osteocyte lacunar-canalicular network associated bone matrix revealed by quantitative nanomechanical mapping. Nano Res. 8, 3250–3260.